Spin-Degeneracy Breaking and Parity Transitions in Three-Terminal Josephson Junctions

M. Coraiola,[1] D. Z. Haxell,[1] D. Sabonis,[1] M. Hinderling,[1] S. C. ten Kate,[1] E. Cheah,[2] F. Krizek,[1,2,†] R. Schott,[2] W. Wegscheider,[2] and F. Nichele[1,*]

[1]*IBM Research Europe-Zurich, 8803 Rüschlikon, Switzerland*
[2]*Laboratory for Solid State Physics, ETH Zürich, 8093 Zürich, Switzerland*

(Received 17 August 2023; accepted 2 July 2024; published 13 August 2024)

Hybrid Josephson junctions (JJs) realized in superconductor-semiconductor heterostructures host fermionic modes known as Andreev bound states (ABSs). In these structures, a promising and yet unexplored avenue for harnessing spin and parity degrees of freedom is offered by JJs with three or more superconducting terminals, where phase-induced spin polarization and transitions of the ground state to an odd parity were predicted to arise. Here we spectroscopically probe the two-dimensional band structure of ABSs in a phase-controlled InAs/Al three-terminal JJ. Andreev bands show signatures of spin-degeneracy breaking, with level splitting in excess of ∼9 GHz, and zero-energy crossings associated to ground state fermion parity transitions. Spin splitting and parity transitions are enabled and controlled by locally applied magnetic fluxes, in the absence of Zeeman effect or Coulomb blockade. Our results underscore the potential of multiterminal hybrid devices for phase engineering ABSs, with significant implications for spin- and parity-based quantum devices.

DOI: 10.1103/PhysRevX.14.031024

Subject Areas: Condensed Matter Physics, Mesoscopics, Superconductivity

The spin of quantum particles offers an ideal basis for two-level systems, enabling spin qubit-based quantum information processing [1,2]. Access to spin-resolved states, typically confined in semiconducting quantum dots, requires breaking of the time-reversal symmetry to lift the Kramers degeneracy, often achieved via large magnetic fields. The combination of semiconductors and superconductors into hybrid material platforms [3,4] creates unprecedented opportunities for spin manipulation with Andreev bound states (ABSs)—fermionic modes arising in a semiconducting region bounded by superconductors [5–13]. Previously, resolving spin-split ABSs was attained in large magnetic fields (∼100 mT) [14,15] or by integration of ferromagnetic elements [16–18]. An interesting route to locally break time-reversal symmetry without the need for these ingredients is via control over the superconducting phase difference, although it normally requires long Josephson junctions (JJs) with strong spin-orbit coupling (SOC) to lift the spin degeneracy [19–22]. This led to measured level splittings up to ∼1 GHz [23–25] and enabled the realization of Andreev spin qubits [19,22,26–29], that leverage the advantages of both superconducting and spin qubit platforms.

Multiterminal JJs with SOC offer intriguing prospects for superconducting spin manipulation [30]: in such devices, large spin splitting may be induced solely by controlling superconducting phase differences, while remaining in the short-junction limit. Concomitantly, ground state fermion parity transitions (i.e., switches between even and odd number of fermions in the superconducting condensate) are expected, marked by zero-energy Andreev level crossings in the spectrum [31]. Parity engineering is of crucial importance for realizing artificial Kitaev chains [32–35] and parity-protected qubits [36–39]. Unlike their two-terminal counterparts, multiterminal JJs enable parity tuning in the absence of charging energies and external magnetic fields [30]. Transport properties of multiterminal devices have been the subject of intense investigation [40–52]. Recent experiments revealing ABS spectra in phase-controlled three-terminal JJs (3TJJs) [53] provided a first demonstration of higher-dimensional Andreev band structures [54–56], particularly in the context of Andreev molecules [57–62], but the feasibility of spin-resolved ABSs is yet to be established.

Here we report on spectroscopic measurements of planar 3TJJs with SOC. Andreev bound state spectra are consistent with spin-degeneracy breaking and parity transitions, controlled by superconducting phase differences. We observe large ABS spin splitting (approximately 38 μeV,

*Contact author: fni@zurich.ibm.com
†Present address: Institute of Physics, Czech Academy of Sciences, 162 00 Prague, Czech Republic.

corresponding to a frequency in excess of 9 GHz) and level crossings at zero energy, indicating ground state fermion parity transitions. These phenomena are realized in the absence of Zeeman magnetic fields or Coulomb blockade. *In situ* spin and parity tuning is enabled by phase control through integrated flux-bias lines. The spin nature of the splitting is further supported by magnetic field-dependent studies. We discuss our experimental observations in the light of theoretical work on multiterminal JJs. These results demonstrate a new approach for engineering spin and parity degrees of freedom in hybrid quantum devices.

A schematic representation of a hybrid 3TJJ is displayed in Fig. 1(a): Three superconducting terminals, with phases ϕ_L, ϕ_R, and ϕ_M, are coupled to a normal scattering region $\mathcal{S}$. Because of gauge invariance, we set $\phi_M \equiv 0$; hence, ϕ_L and ϕ_R correspond to the two independent superconducting phase differences. As derived in Ref. [30] in the short-junction limit, the necessary condition for a zero-energy ABS to exist in the spectrum is that the phases of the terminals wind by 2π around the junction. This is referred to as the "discrete vortex condition" and is geometrically illustrated in Fig. 1(b). Assigning to each phase ϕ_α (where $\alpha \in \{L, R, M\}$) the point $ie^{i\phi_\alpha}$ on the complex plane, the condition is fulfilled when the area of the resulting triangle covers the origin (as shown, for example, by the red triangle). In this case, the ground state fermion parity can switch from even to odd, and a zero-energy Andreev level crossing marks the transition. If the condition is not fulfilled (e.g., gray triangle), the parity of the system remains even, and the ABS energy cannot reach zero but has a finite lower bound. In the two-dimensional (2D) phase space, values of (ϕ_L, ϕ_R) for which a discrete vortex is present in the 3TJJ (i.e., odd fermion parity is allowed) describe a pair of triangular regions [red in Fig. 1(c)]. We note that when any phase difference is zero ($\phi_L = 0$, $\phi_R = 0$, or $\phi_L = \phi_R$), the system behavior is reduced to that of a two-terminal JJ and its parity has to stay even, except at the points where the other phase difference is $\phi = \pi$. However, in a real junction with nonunity transmission τ, ABSs never reach zero energy; thus the gap cannot close and no parity transition may occur. Rather, ABSs described by the energy-phase dispersion relation [63],

$$E_A(\phi) = \pm\Delta\sqrt{1 - \tau\sin^2(\phi/2)}, \tag{1}$$

valid in the short-junction limit, have minimum energy $|E_A(\pi)| = \Delta\sqrt{1-\tau}$, where Δ is the induced superconducting gap. This corresponds to the spectrum plotted in Fig. 1(d) as a function of $\phi \equiv \phi_L = \phi_R$ [cyan line in Fig. 1(c)]. Importantly, we remark that ABSs must remain spin degenerate in this configuration, even if spin-rotation symmetry is broken by SOC in the 3TJJ. A different scenario unfolds when $\phi_L \neq \phi_R$ (both finite): In this case, if SOC is present, the spin degeneracy of the spectrum can be lifted, leading to a large spin splitting up to a significant fraction of Δ. In addition, ABSs are allowed to cross at zero energy forming

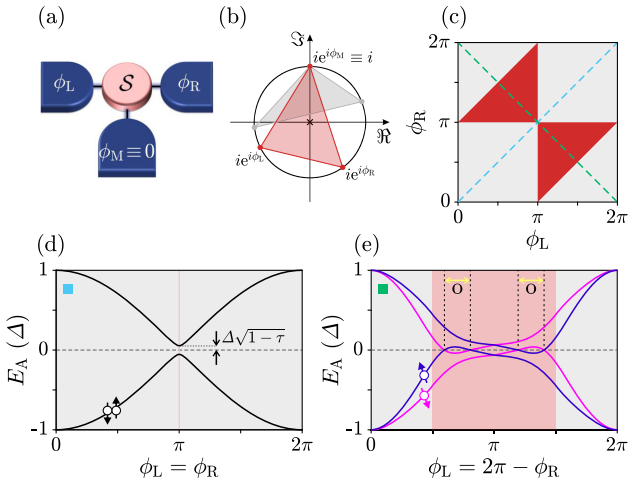

FIG. 1. (a) Schematic representation of a hybrid three-terminal Josephson junction (3TJJ). Three superconducting leads with phases ϕ_L, ϕ_R, and $\phi_M \equiv 0$ are coupled to a common scattering region $\mathcal{S}$. (b) Geometric illustration of the discrete vortex condition, i.e., the necessary condition for the occurrence of zero-energy Andreev bound states (ABSs) and ground state fermion parity transitions. A triangle with vertices $ie^{i\phi_\alpha}$ (for $\alpha \in \{L, R, M\}$) is defined on the unitary circle in the complex plane. If it covers the origin (red triangle), the phases wind by 2π around the 3TJJ and the discrete vortex condition is fulfilled. Otherwise (gray triangle), zero-energy ABSs and parity transitions are not allowed (adapted from Ref. [30]). (c) Parity diagram in the two-dimensional phase space, spanned by the superconducting phase differences ϕ_L and ϕ_R. In the red regions, the discrete vortex condition is fulfilled and parity transitions are allowed, whereas parity must stay even in the gray regions. Dashed cyan and green lines indicate the phase-space line cuts $\phi_L = \phi_R$ and $\phi_L = 2\pi - \phi_R$, respectively. (d) Energy-phase ABS dispersion along $\phi_L = \phi_R$, corresponding to a conventional, spin-degenerate ABS described by Eq. (1). Fermion parity of the ground state must remain even (gray shading). Nonperfect transmission $\tau = 0.997$ is assumed, which prevents ABSs from reaching zero energy at π phase. (e) Dispersion of ABSs along $\phi_L = 2\pi - \phi_R$ (schematic representation adapted from Ref. [30]). Spin degeneracy is lifted due to the combination of superconducting phases and spin-orbit coupling in $\mathcal{S}$. Blue and magenta ABSs have opposite spin character. The red shading designates the phase range where transitions from even to odd parity are allowed. Odd-parity regions (o) are delimited by zero-energy Andreev level crossings and are indicated by the yellow arrows.

extended regions of odd ground state fermion parity [30]. Both effects are visible in the spectrum of Fig. 1(e), shown along the phase-space line cut $\phi_L = 2\pi - \phi_R$ [green in Fig. 1(c)].

To investigate these phenomena, we realized a 3TJJ in an InAs/Al heterostructure [4,64], simultaneously exploiting the strong Rashba SOC in the InAs 2D electron gas (2DEG) and the scalable, top-down patterning approach offered by the heterostructure material. The device, displayed in Fig. 2, features three superconducting terminals (L, M, and R), defined by selective etching of the Al layer and

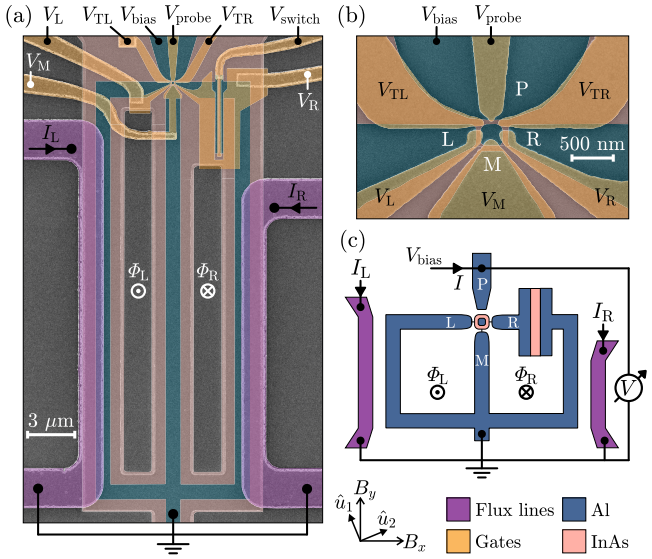

FIG. 2. (a) False-colored scanning electron micrograph of a device identical to that under study. Selective removal of Al (blue) exposes the III-V semiconductor below (pink), before being uniformly covered by a dielectric layer (not visible). Gates (yellow) and flux-bias lines (purple) are patterned on top of the dielectric. (b) Enlargement of (a) near the three-terminal Josephson junction region. (c) Schematic of the device together with the measurement setup. Tunneling spectroscopy is performed by measuring the current I flowing through the superconducting probe P (biased by voltage V_{bias}) and the voltage V across the device with lock-in techniques, to obtain the differential conductance G. Independent control over two superconducting phase differences is enabled by the flux-line currents I_{L} and I_{R}, that generate external magnetic fluxes Φ_{L} and Φ_{R} threading the two superconducting loops. An in-plane magnetic field can be applied with a vector magnet. B_x and B_y directions are indicated, as well as $\hat{u}_2$ and $\hat{u}_1$ that are rotated by 22.5° counterclockwise.

coupled to a common scattering region, forming a 3TJJ. The dimensions of this region, $300 \times 250\ \mathrm{nm}^2$, were chosen to be relatively large on the scale of the spin-orbit length in InAs, $l_{\mathrm{SO}} \sim 150$ nm [65], yet substantially smaller than the superconducting coherence length of proximitized InAs, $\xi_{\mathrm{InAs}} \sim 600$ nm. As a result, the effect of SOC is expected to be appreciable in the 3TJJ (unlike the implementation described by Ref. [53]). Compared to the system studied in Ref. [30], that was simulated assuming the short-junction limit and a diameter of the 3TJJ 10 times larger than l_{SO}, our device has finite size with respect to ξ_{InAs} and lower SOC strength. In the middle of the scattering region, a superconducting island of diameter of 200 nm is left for two main purposes: First, it screens stray electric fields and prevents uncontrolled depletion of the 3TJJ from the gates, hence supporting the formation of high-transmission channels below it; second, the island facilitates uniform coupling of all terminals to the scattering region, enabling ABSs to depend on all superconducting phases. In particular, a direct conducting channel is observed to form between terminals L and R despite their larger separation compared to L-M and M-R, likely aided by the presence of the superconducting island (see discussion below and in the Supplemental Material [66], Sec. VI). The small size of the island with respect to ξ_{InAs} (that is, the length scale governing ABS hybridization through the common proximitized region [61]) prevents the formation of independent two-terminal JJs between each terminal and the island itself. The three leads L, M, and R are connected to a common node defining two closed superconducting loops, which allow for independent tuning of two phases [53]. A JJ integrated on R (referred to as "switch JJ"), with a length of 40 nm and a width of 5 μm, was designed to have a critical current much larger than between any pairs of L, M, and R; therefore, the phases of the 3TJJ are not influenced by it. The presence of the switch JJ does not affect the following discussion, and a description of its effect is provided in Ref. [66]. A fourth superconducting terminal (P), biased by the dc voltage V_{bias}, served as a probe to perform tunneling spectroscopy of subgap states in the 3TJJ. Metallic gate electrodes and flux-bias lines were patterned on top of a dielectric layer, uniformly deposited across the entire sample. Gates energized by the voltages V_{TL} and V_{TR} were both set to $V_{\mathrm{T}} = -1.285$ V to deplete the 2DEG below and form a tunneling contact between P and the 3TJJ (see Fig. S1 [66] for a full dependence on V_{T}). In such a weak-coupling regime, the influence of the probe on the rest of the circuit can be neglected and the differential conductance G, measured between P and the common node with low-frequency lock-in techniques [see Fig. 2(c)], is proportional to the convolution between the density of states (DOS) of the probe and the DOS of the 3TJJ weighted by the transmission of the tunneling contact [7,13,67]. Assuming a Bardeen-Cooper-Schrieffer-like DOS for the superconducting probe, which peaks at energy $\pm\Delta$, the differential conductance exhibits a peak at bias voltage $(\Delta + E)/e$ for a peak in the DOS of the 3TJJ at energy $E > 0$, or at voltage $(-\Delta + E)/e$ for $E < 0$. Gates covering the normal regions between the island and the three superconducting terminals were kept at $V_{\mathrm{L}} = V_{\mathrm{M}} = V_{\mathrm{R}} = 0$ and had the main role of screening the effect of the other gates on the scattering region, without introducing a charging energy. Two additional gates were set to $V_{\mathrm{probe}} = 0.42$ V and $V_{\mathrm{switch}} = 0$ throughout. Currents I_{L} and I_{R} injected into the flux-bias lines generated external magnetic fluxes Φ_{L} and Φ_{R} threading the superconducting loops and enabled full control over the 2D phase space. Experiments were performed in a dilution refrigerator with base temperature below 10 mK, equipped with a three-axis vector magnet. Magnetic field directions B_x and B_y are indicated in Fig. 2, together with the additional orientations $\hat{u}_1$ and $\hat{u}_2$ (rotated by 22.5° counterclockwise with respect to B_y and B_x, respectively). Further details regarding materials, fabrication, and measurement setup are provided in Ref. [66] (Sec. I).

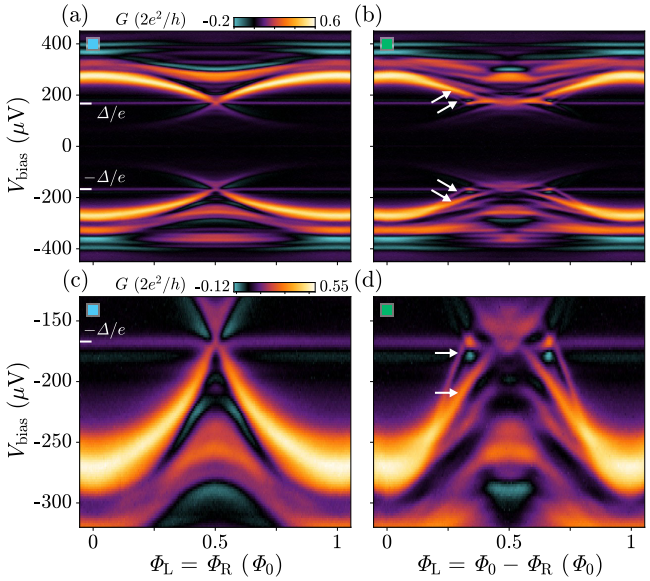

FIG. 3. Tunneling spectroscopy of Andreev bound states along phase-space line cuts. (a) Differential tunneling conductance G as a function of voltage bias $V_{\rm bias}$ along line cut $\Phi_L = \Phi_R$, revealing a high-transmission ABS with conventional phase dispersion. Because of the superconducting probe, a transport gap between $V_{\rm bias} = \pm\Delta/e = \pm 167$ μV is present in the spectrum. (b) G as a function of $V_{\rm bias}$ along line cut $\Phi_L = \Phi_0 - \Phi_R$. The ABS spectrum is strongly modified compared to (a), showing level splitting, compatible with spin-degeneracy breaking, and zero-energy crossings (highlighted by the conductance enhancement at $|V_{\rm bias}| = \Delta/e$) marking ground state parity transitions in the spectrum. (c),(d) Enlargement of (a),(b) on the ABS spectrum at negative $V_{\rm bias}$. The white arrows indicate the spin-split Andreev levels discussed in the text.

Tunneling spectroscopy measurements of phase-dispersing ABSs are shown in Fig. 3. The spectra are probed as a function of $V_{\rm bias}$ along the two flux-space line cuts $\Phi_L = \Phi_R$ [Figs. 3(a) and 3(c)] and $\Phi_L = \Phi_0 - \Phi_R$ [Figs. 3(b) and 3(d)], obtained from linear combinations of the flux-line currents I_L and I_R [see also Fig. 4(a), and Fig. S2 [66] for the dependence on Φ_L and Φ_R]. Here, $\Phi_0 = h/2e$ is the superconducting flux quantum, with h the Planck constant and e the elementary charge. These line cuts correspond to those introduced in Figs. 1(c)–1(e) for the 2D phase space (cyan and green line, respectively). All measurements show a transport gap of $2\Delta/e = 334$ μV introduced by the superconducting probe, bounded by differential conductance peaks at $V_{\rm bias} = \pm 167$ μV with negligible flux dependence. Above the transport gap, the spectrum is dominated by flux-dependent resonances, representing ABSs in the 3TJJ [7,13,53]. The main spectral features are symmetric about $V_{\rm bias} = 0$, compatible with a particle-hole symmetric DOS, while their linewidth and conductance amplitude display some asymmetry, with the features being sharper for $V_{\rm bias} < 0$. An asymmetry in the differential conductance might be related to a bias voltage-dependent transmission of the tunneling contact, and to direct gating of the 3TJJ normal region by the voltage applied to the probe. Furthermore, since the device is not spatially symmetric along the direction of the current flow, it may not exhibit symmetric current-to-voltage characteristics for positive and negative $V_{\rm bias}$. Regions of negative differential conductance are visible in the data and characteristic of superconductor-insulator-superconductor spectroscopy [13,67]. Finite conductance features within the transport gap are ascribed to a nonzero DOS in the superconducting probe for energies $|E| \lesssim \Delta$, presumably due to a combination of quasiparticle-lifetime broadening [68] and high-energy subgap bound states forming on the probe side of the tunneling contact. The spectrum shown in Figs. 3(a) and 3(c) reveals an ABS resembling the conventional energy dispersion of Eq. (1) with near-unity transmission, as it forms a sharp cusp that approaches the transport gap edge very closely. We note that the state does not reach $e|V_{\rm bias}| = 2\Delta/e$ at $\Phi_L = \Phi_R = 0, \Phi_0$, which might be attributed to the finite dimensions of the 3TJJ on the scale of $\xi_{\rm InAs}$ [Eq. (1) is valid in the short-junction limit]. Alternatively, ABS repulsion from $\pm\Delta$ could be ascribed to the interaction with high-energy subgap states forming at the individual leads and, thus, independent of applied magnetic fluxes.

Conversely, the spectrum probed along $\Phi_L = \Phi_0 - \Phi_R$ [Figs. 3(b) and 3(d)] exhibits a striking difference from that of Eq. (1): As the ABS moves from high $|V_{\rm bias}|$ toward $e|V_{\rm bias}| = \Delta$, it markedly splits into two resonances (white arrows). Both appear to fully reach $e|V_{\rm bias}| = \Delta$; i.e., the split ABSs cross zero energy. This is more evident for the outermost ABS, that overlaps with $e|V_{\rm bias}| = \Delta$ at a flux significantly different from $\Phi_L = 0.5\Phi_0$, resulting in a point of enhanced conductance; concomitantly, the slope of the state dispersion has a sharp change of sign at the crossing point.

Next, we map the 2D phase space by performing tunneling spectroscopy at fixed values of $V_{\rm bias}$ as a function of both I_L and I_R, resulting in constant-energy cut planes of the Andreev band structure. In Fig. 4(a), where $eV_{\rm bias} = -\Delta - 20$ μeV $= -187$ μeV, the phase space is scanned over an extended region, showing periodicity along two main directions (white lines) that correspond to the external fluxes Φ_L and Φ_R, defined in Fig. 2. The dashed cyan and green segments represent the $\Phi_L = \Phi_R$ and $\Phi_L = \Phi_0 - \Phi_R$ line cuts displayed in Fig. 3. Two high-transmission ABSs, dispersing with Φ_L and Φ_R, respectively, form avoided crossings around the $(\Phi_0/2 + n\Phi_0, \Phi_0/2 + m\Phi_0)$ points (with n, m integers), which indicates ABS hybridization and the formation of a phase-dependent Andreev molecule [53]. Furthermore, we note additional split lines (turquoise arrows)—only encountered along $\Phi_L = \Phi_0 - \Phi_R$ and whose paths on the phase space depend on both Φ_L and Φ_R—that are the split ABSs described for Figs. 3(b) and 3(d). To study zero-energy Andreev level crossings in the phase space, we set $V_{\rm bias} = -167$ μV (i.e., $eV_{\rm bias} + \Delta = 0$), resulting in the cut

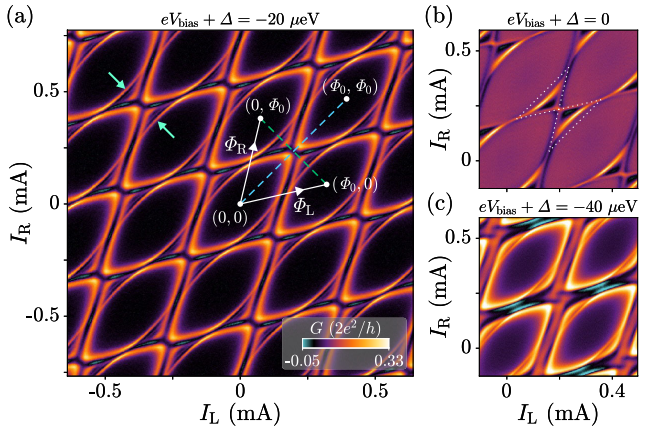

FIG. 4. Constant-energy cut planes of the Andreev band structure measured in the two-dimensional phase space. (a) Differential tunneling conductance G as a function of flux-line currents $I_{\rm L}$ and $I_{\rm R}$ at fixed voltage bias $V_{\rm bias}$, such that $eV_{\rm bias} + \Delta = -20$ μeV (with $\Delta = 167$ μeV), resulting in a cut plane 20 μeV below the Fermi level. Periodicity along two directions, corresponding to the external magnetic fluxes $\Phi_{\rm L}$ and $\Phi_{\rm R}$, is highlighted by the white segments. Dashed cyan and green lines indicate the phase-space line cuts $\Phi_{\rm L} = \Phi_{\rm R}$ and $\Phi_{\rm L} = \Phi_0 - \Phi_{\rm R}$, shown in Fig. 3, and correspond to the paths $\phi_{\rm L} = \phi_{\rm R}$ and $\phi_{\rm L} = 2\pi - \phi_{\rm R}$ plotted in Fig. 1(c). Split lines marked by the turquoise arrows are related to the spin-split Andreev levels visible in the spectrum [Figs. 3(b) and 3(d)]. (b) As (a), but measured at $eV_{\rm bias} + \Delta = 0$ to probe the Andreev band structure at zero energy. Conductance peaks are zero-energy Andreev level crossings in the spectrum, corresponding to transitions in the ground state parity of the system, and thus enclose regions of odd parity. These are comprised in the phase-space regions where the discrete vortex condition is verified [red in Fig. 1(c), reported here as the dotted white triangles]. (c) As (a), but at $eV_{\rm bias} + \Delta = -40$ μeV, showing the Andreev band structure at higher energy.

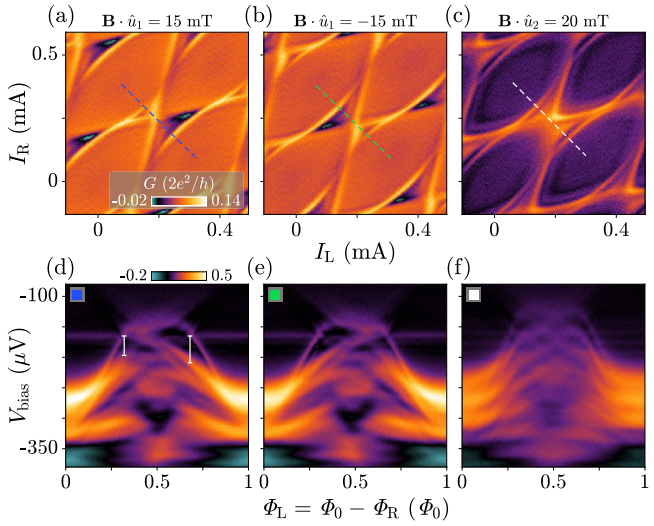

FIG. 5. Effect of an in-plane magnetic field on the Andreev bound state spectrum. (a) Differential tunneling conductance G as a function of flux-line currents $I_{\rm L}$ and $I_{\rm R}$ at fixed voltage bias $V_{\rm bias} = -167$ μV, with an in-plane magnetic field $\mathbf{B}$ of magnitude of 15 mT applied along the direction of $\hat{u}_1$ [see Fig. 2]. The strong asymmetry in the ABS features is attributed to the alignment of $\mathbf{B}$ with the spin-orbit field $\mathbf{B}_{\rm SO}$ and indicates that the split lines originate from the spin degree of freedom. (b) As (a), but reversing the direction of $\mathbf{B}$, which causes the inversion of all features with respect to $\Phi_{\rm L} = \Phi_{\rm R} = \Phi_0/2$. (c) As (a), but applying a magnetic field of 20 mT along $\hat{u}_2$ (orthogonal to $\hat{u}_1$) and at $V_{\rm bias} = -157$ μV. Symmetry of the features is compatible with $\mathbf{B} \perp \mathbf{B}_{\rm SO}$. (d) Conductance G as a function of $V_{\rm bias}$ along the $\Phi_{\rm L} = \Phi_0 - \Phi_{\rm R}$ line cut [dashed blue line in (a)], for a magnetic field of 15 mT along $\hat{u}_1$, revealing the asymmetry in the ABS spectrum. White bars indicate the spin splitting at $\Phi_{\rm L} = \Phi_0 - \Phi_{\rm R} = 0.32\Phi_0$ and $0.68\Phi_0$. (e) As (d), but reversing $\mathbf{B}$. Spectral ABS features are reversed. (f) As (d), but with a magnetic field of 20 mT applied along $\hat{u}_2$. The spectrum symmetry is consistent with the cut plane in (c).

plane of Fig. 4(b). Here, we observe conductance resonances defining pairs of triangles, which are within the phase space areas fulfilling the discrete vortex condition [red triangles in Fig. 1(c), whose perimeter is reported as the dotted white triangles in Fig. 4(b)]. Finally, Fig. 4(c) shows the cut plane at $eV_{\rm bias} + \Delta = -40$ μeV, revealing the evolution of the high-transmission ABSs and of the split lines at higher bias, and the occurrence of an additional ABS with lower transmission in the spectrum. More cut planes for varying $V_{\rm bias}$ are presented in Ref. [66] (see Fig. S3 [66]), as well as the conversion from the flux-line-current axes $(I_{\rm L}, I_{\rm R})$ to the flux axes $(\Phi_{\rm L}, \Phi_{\rm R})$ (see Fig. S11 [66]).

To further investigate the origin of the splitting identified in Figs. 3 and 4, we measure additional constant-energy planes and ABS spectra along the $\Phi_{\rm L} = \Phi_0 - \Phi_{\rm R}$ direction while an external in-plane magnetic field $\mathbf{B}$ is applied to the device. Rashba SOC in InAs is expected to result in an in-plane spin-orbit field $\mathbf{B}_{\rm SO}$ perpendicular to the direction of motion [69]; however, since the geometry of the 3TJJ does not impose a preferential direction for transport, we cannot make assumptions regarding the orientation of $\mathbf{B}_{\rm SO}$. Instead, we perform a coarse angle dependence of $\mathbf{B}$ and identify directions $\hat{u}_1$ and $\hat{u}_2$ that are inferred to be approximately parallel and orthogonal to $\mathbf{B}_{\rm SO}$ based on the symmetry of the resulting spectrum (see Ref. [66], Sec. VIII for additional orientations of the in-plane magnetic field). When $\mathbf{B} \| \hat{u}_1$ [Figs. 5(a) and 5(d)], we observe a pronounced asymmetry in both the triangular features at zero energy [Fig. 5(a)] and the split ABS spectrum [Fig. 5(d)], as expected from spin-orbit-split states in the case that $\mathbf{B}$ has a large component along $\mathbf{B}_{\rm SO}$ [21–23,70]. Compared to the zero-field case, ABSs appear to smoothly cross the flux-independent line, consistent with the softening of the superconducting gap of the probe caused by the applied magnetic field [71]. Notably, the splitting is enhanced on one side of the line cut ($\Phi_{\rm L} = \Phi_0 - \Phi_{\rm R} > 0.5\Phi_0$) and reduced on the other side, consistent with the Zeeman effect. For example, at fluxes $0.32\Phi_0$ and

$0.68\Phi_0$—where the maximum zero-field splitting of approximately 38 μV is observed in Figs. 3(b) and 3(d)—the two spin levels are split by about 32 and 44 μV, respectively [see white bars in Fig. 5(d)]. Assuming $\mathbf{B}\|\mathbf{B}_{\mathrm{SO}}$ and $|\mathbf{B}| \ll |\mathbf{B}_{\mathrm{SO}}|$, the Zeeman splitting $E_{\mathrm{Z}} = g^*\mu_{\mathrm{B}}|\mathbf{B}|$ (where g^* is the effective g factor in InAs and μ_{B} the Bohr magneton) is added to or subtracted from the zero-field spin-orbit-induced splitting, thus yielding $E_{\mathrm{Z}} \approx 6$ μeV and $g^* \approx 7$, comparable to previous observations [72]. By further considering a Rashba coefficient $\alpha \sim 2.2 \times 10^{-11}$ eV m [65] and an electron sheet density $n_{\mathrm{s}} = 8 \times 10^{11}$ cm^{-2} (see Ref. [66], Sec. I), we estimate $|\mathbf{B}_{\mathrm{SO}}| = \alpha\sqrt{8\pi n_{\mathrm{s}}}/g^*\mu_{\mathrm{B}} \sim 24$ T. Furthermore, we verify that all spectral features of Figs. 5(a) and 5(d) are flipped around $\Phi_{\mathrm{L}} = \Phi_{\mathrm{R}} = \Phi_0/2$ upon inversion of the magnetic field direction, as seen in Figs. 5(b) and 5(e). Conversely, an asymmetry is not expected when the field is applied orthogonal to $\mathbf{B}_{\mathrm{SO}}$, which is approximately the situation of Figs. 5(c) and 5(f) for $\mathbf{B}\|\hat{u}_2$.

The measurements presented in Figs. 3(b) and 3(d) display the two key signatures of the spectra predicted by Ref. [30], schematically summarized in Fig. 1(e): ABS splitting and zero-energy crossings. We thus interpret the former as spin-degeneracy breaking, and the latter as fermion parity transitions in the ground state of the system 31]]. We note that our device is not an exact realization of the theoretical proposal and, in line with the additional complexity and different parameter regime of the experimental platform, some details of the measured spectra deviate from the simulations. Nevertheless, to the best of our knowledge, the model proposed in Ref. [30] offers the most suitable theoretical description of the system under study. The essential ingredients of the model are present in our realization, which motivates its use as a framework to interpret the main experimental signatures. The two effects that we report, occurring in the absence of Zeeman magnetic fields, are a direct manifestation of the Andreev band structure of a 3TJJ with Rashba SOC, and are enabled by control over two superconducting phase differences. Experimentally, such control via flux-bias lines is local and allows for wide tunability of the spin-splitting size and of the parity of the system. In our data, we observe a maximum energy splitting of about 38 μeV, corresponding to a frequency of over 9 GHz and to 0.22Δ (for an induced superconducting gap of $\Delta = 167$ μeV), that is approximately one order of magnitude larger than what has been achieved in long JJs based on nanowires with SOC [23,28] and aligns to the theoretical prediction [30]. The cut planes of the Andreev band structure at constant energy (Fig. 4) show the trajectories of spin-split ABSs and of zero-energy crossings in the 2D phase space. In Fig. 4(b), the triangles enclosed by the zero-energy conductance peaks represent regions where the ground state fermion parity has transitioned from even to odd, fulfilling the discrete vortex condition. Measurements in an in-plane magnetic field display an anisotropic behavior, with a pronounced asymmetry and an enhanced splitting when $\mathbf{B}$ is inferred to be approximately aligned with $\mathbf{B}_{\mathrm{SO}}$. This further indicates that the origin of the splitting is related to the spin degree of freedom.

The results discussed thus far were acquired with no tuning of the 3TJJ gates, i.e., at $V_{\mathrm{L}} = V_{\mathrm{M}} = V_{\mathrm{R}} = 0$. Additional gate configurations are presented in Figs. S5–S10 [66], showing the effect of individual gates and indicating that the main spectroscopic features are still present regardless of the specific tuning. Importantly, key features such as ABS level splitting and zero-energy crossings are visible only when all three terminals are coupled to the scattering region. These data also reveal the presence of a high-transmission conductive channel between each pair of terminals. By comparing with a previous realization [53], we deduce that the superconducting island constitutes an experimentally crucial ingredient to enable this situation, in particular, to have a channel between the terminals with the largest separation (which was not observed in Ref. [53]). Spectral signatures similar to those presented here were also measured on a second device (see Figs. S14 and S15 [66]).

In summary, we investigated ABS spectra in a phase-controlled 3TJJ with SOC via tunneling spectroscopy experiments. Independent control over two superconducting phase differences enabled access to the Andreev band structure in the 2D phase space. We observed ABS splitting, compatible with breaking of the spin degeneracy, and zero-energy Andreev level crossings, indicating ground state fermion parity transitions. Theoretical predictions for multiterminal JJs with SOC [30] were considered to support our interpretation. In the phase space probed at zero energy, odd-parity regions were enclosed by contours of conductance peaks forming pairs of triangles, fulfilling the necessary condition for parity transitions, namely the presence of a discrete vortex in the 3TJJ. Both effects—spin splitting and parity transitions—arise without the need for Zeeman magnetic fields or Coulomb blockade, and are tuned by controlling superconducting phase differences. The size of the observed splitting (up to approximately 38 μeV, or over 9 GHz) is substantially larger than previously reported values in nanowire-based long JJs. These results demonstrate that spin and parity degrees of freedom of quantum states are widely controllable by phase tuning in multiterminal hybrid nanostructures. An immediate application is the realization of superconducting spin qubits benefiting from a large, phase-tunable spin-level splitting at zero external fields. Parity control in open systems could be exploited for the engineering of topologically protected Kitaev chains and parity-protected qubits. The access to transition frequencies between spin-resolved levels of several gigahertz makes our devices ideal for integration with circuit quantum electrodynamics architectures, while *in situ* and fast frequency tuning via

integrated flux-bias lines will potentially enable high-performance logic and multiqubit coupling schemes.

The data that support the findings of this article are openly available [73].

We acknowledge fruitful discussions with W. Belzig, J. C. Cuevas, J. Klinovaja, H. Legg, D. Loss, A. E. Svetogorov, and H. Weisbrich. We are grateful to B. van Heck for useful comments on the manuscript. We thank the Cleanroom Operations Team of the Binnig and Rohrer Nanotechnology Center (BRNC) for their help and support. W. W. acknowledges support from the Swiss National Science Foundation (Grant No. 200020_207538). F. N. acknowledges support from the European Research Council (Grant No. 804273) and the Swiss National Science Foundation (Grant No. 200021_201082).

F. N. conceived the experiment. E. C., F. K., R. S., and W. W. developed and provided the heterostructure material. Devices were designed by M. C. and fabricated by M. C. and D. Z. H. M. C. and F. N. performed the electrical measurements and interpreted the data, with input from D. Z. H., D. S., M. H., and S. C. t. K. M. C wrote the manuscript with feedback from all of the authors.

[1] D. Loss and D. P. DiVincenzo, *Quantum computation with quantum dots*, Phys. Rev. A **57**, 120 (1998).
[2] G. Burkard, T. D. Ladd, A. Pan, J. M. Nichol, and J. R. Petta, *Semiconductor spin qubits*, Rev. Mod. Phys. **95**, 025003 (2023).
[3] P. Krogstrup, N. L. B. Ziino, W. Chang, S. M. Albrecht, M. H. Madsen, E. Johnson, J. Nygård, C. M. Marcus, and T. S. Jespersen, *Epitaxy of semiconductor–superconductor nanowires*, Nat. Mater. **14**, 400 (2015).
[4] J. Shabani, M. Kjaergaard, H. J. Suominen, Y. Kim, F. Nichele, K. Pakrouski, T. Stankevic, R. M. Lutchyn, P. Krogstrup, R. Feidenhans'l, S. Kraemer, C. Nayak, M. Troyer, C. M. Marcus, and C. J. Palmstrøm, *Two-dimensional epitaxial superconductor–semiconductor heterostructures: A platform for topological superconducting networks*, Phys. Rev. B **93**, 155402 (2016).
[5] C. W. J. Beenakker and H. van Houten, *Josephson current through a superconducting quantum point contact shorter than the coherence length*, Phys. Rev. Lett. **66**, 3056 (1991).
[6] A. Furusaki and M. Tsukada, *Current-carrying states in Josephson junctions*, Phys. Rev. B **43**, 10164 (1991).
[7] J.-D. Pillet, C. H. L. Quay, P. Morfin, C. Bena, A. L. Yeyati, and P. Joyez, *Andreev bound states in supercurrent-carrying carbon nanotubes revealed*, Nat. Phys. **6**, 965 (2010).
[8] W. Chang, V. E. Manucharyan, T. S. Jespersen, J. Nygård, and C. M. Marcus, *Tunneling spectroscopy of quasiparticle bound states in a spinful Josephson junction*, Phys. Rev. Lett. **110**, 217005 (2013).
[9] L. Bretheau, Ç. Ö. Girit, H. Pothier, D. Esteve, and C. Urbina, *Exciting Andreev pairs in a superconducting atomic contact*, Nature (London) **499**, 312 (2013).
[10] L. Bretheau, Ç. Ö. Girit, C. Urbina, D. Esteve, and H. Pothier, *Supercurrent spectroscopy of Andreev states*, Phys. Rev. X **3**, 041034 (2013).
[11] C. Janvier, L. Tosi, L. Bretheau, C. O. Girit, M. Stern, P. Bertet, P. Joyez, D. Vion, D. Esteve, M. F. Goffman, H. Pothier, and C. Urbina, *Coherent manipulation of Andreev states in superconducting atomic contacts*, Science **349**, 1199 (2015).
[12] M. Hays, G. de Lange, K. Serniak, D. J. van Woerkom, D. Bouman, P. Krogstrup, J. Nygård, A. Geresdi, and M. H. Devoret, *Direct microwave measurement of Andreev-bound-state dynamics in a semiconductor-nanowire Josephson junction*, Phys. Rev. Lett. **121**, 047001 (2018).
[13] F. Nichele, E. Portolés, A. Fornieri, A. M. Whiticar, A. C. C. Drachmann, S. Gronin, T. Wang, G. C. Gardner, C. Thomas, A. T. Hatke, M. J. Manfra, and C. M. Marcus, *Relating Andreev bound states and supercurrents in hybrid Josephson junctions*, Phys. Rev. Lett. **124**, 226801 (2020).
[14] E. J. H. Lee, X. Jiang, M. Houzet, R. Aguado, C. M. Lieber, and S. D. Franceschi, *Spin-resolved Andreev levels and parity crossings in hybrid superconductor–semiconductor nanostructures*, Nat. Nanotechnol. **9**, 79 (2014).
[15] D. J. van Woerkom, A. Proutski, B. van Heck, D. Bouman, J. I. Väyrynen, L. I. Glazman, P. Krogstrup, J. Nygård, L. P. Kouwenhoven, and A. Geresdi, *Microwave spectroscopy of spinful Andreev bound states in ballistic semiconductor Josephson junctions*, Nat. Phys. **13**, 876 (2017).
[16] J. D. Sau, R. M. Lutchyn, S. Tewari, and S. Das Sarma, *Generic new platform for topological quantum computation using semiconductor heterostructures*, Phys. Rev. Lett. **104**, 040502 (2010).
[17] S. D. Escribano, E. Prada, Y. Oreg, and A. L. Yeyati, *Tunable proximity effects and topological superconductivity in ferromagnetic hybrid nanowires*, Phys. Rev. B **104**, L041404 (2021).
[18] S. Vaitiekėnas, R. S. Souto, Y. Liu, P. Krogstrup, K. Flensberg, M. Leijnse, and C. M. Marcus, *Evidence for spin-polarized bound states in semiconductor–superconductor–ferromagnetic-insulator islands*, Phys. Rev. B **105**, L041304 (2022).
[19] N. M. Chtchelkatchev and Y. V. Nazarov, *Andreev quantum dots for spin manipulation*, Phys. Rev. Lett. **90**, 226806 (2003).
[20] B. Béri, J. H. Bardarson, and C. W. J. Beenakker, *Splitting of Andreev levels in a Josephson junction by spin-orbit coupling*, Phys. Rev. B **77**, 045311 (2008).
[21] A. A. Reynoso, G. Usaj, C. A. Balseiro, D. Feinberg, and M. Avignon, *Spin-orbit-induced chirality of Andreev states in Josephson junctions*, Phys. Rev. B **86**, 214519 (2012).
[22] S. Park and A. L. Yeyati, *Andreev spin qubits in multichannel Rashba nanowires*, Phys. Rev. B **96**, 125416 (2017).
[23] L. Tosi, C. Metzger, M. F. Goffman, C. Urbina, H. Pothier, S. Park, A. L. Yeyati, J. Nygård, and P. Krogstrup, *Spin-orbit splitting of Andreev states revealed by microwave spectroscopy*, Phys. Rev. X **9**, 011010 (2019).
[24] M. Hays, V. Fatemi, K. Serniak, D. Bouman, S. Diamond, G. de Lange, P. Krogstrup, J. Nygård, A. Geresdi, and

M. H. Devoret, *Continuous monitoring of a trapped superconducting spin*, Nat. Phys. **16**, 1103 (2020).

[25] A. Bargerbos, M. Pita-Vidal, R. Žitko, L. J. Splitthoff, L. Grünhaupt, J. J. Wesdorp, Y. Liu, L. P. Kouwenhoven, R. Aguado, C. K. Andersen, A. Kou, and B. van Heck, *Spectroscopy of spin-split Andreev levels in a quantum dot with superconducting leads*, Phys. Rev. Lett. **131**, 097001 (2023).

[26] C. Padurariu and Y. V. Nazarov, *Theoretical proposal for superconducting spin qubits*, Phys. Rev. B **81**, 144519 (2010).

[27] C. Padurariu and Y. V. Nazarov, *Spin blockade qubit in a superconducting junction*, Europhys. Lett. **100**, 57006 (2012).

[28] M. Hays, V. Fatemi, D. Bouman, J. Cerrillo, S. Diamond, K. Serniak, T. Connolly, P. Krogstrup, J. Nygård, A. L. Yeyati, A. Geresdi, and M. H. Devoret, *Coherent manipulation of an Andreev spin qubit*, Science **373**, 430 (2021).

[29] M. Pita-Vidal, A. Bargerbos, R. Žitko, L. J. Splitthoff, L. Grünhaupt, J. J. Wesdorp, Y. Liu, L. P. Kouwenhoven, R. Aguado, B. van Heck, A. Kou, and C. K. Andersen, *Direct manipulation of a superconducting spin qubit strongly coupled to a transmon qubit*, Nat. Phys. **19**, 1110 (2023).

[30] B. van Heck, S. Mi, and A. R. Akhmerov, *Single fermion manipulation via superconducting phase differences in multiterminal Josephson junctions*, Phys. Rev. B **90**, 155450 (2014).

[31] C. W. J. Beenakker, J. M. Edge, J. P. Dahlhaus, D. I. Pikulin, S. Mi, and M. Wimmer, *Wigner-Poisson statistics of topological transitions in a Josephson junction*, Phys. Rev. Lett. **111**, 037001 (2013).

[32] A. Y. Kitaev, *Unpaired Majorana fermions in quantum wires*, Phys. Usp. **44**, 131 (2001).

[33] J. D. Sau and S. D. Sarma, *Realizing a robust practical Majorana chain in a quantum-dot-superconductor linear array*, Nat. Commun. **3**, 964 (2012).

[34] M. Leijnse and K. Flensberg, *Parity qubits and poor man's Majorana bound states in double quantum dots*, Phys. Rev. B **86**, 134528 (2012).

[35] T. Dvir, G. Wang, N. van Loo, C.-X. Liu, G. P. Mazur, A. Bordin, S. L. D. ten Haaf, J.-Y. Wang, D. van Driel, F. Zatelli, X. Li, F. K. Malinowski, S. Gazibegovic, G. Badawy, E. P. A. M. Bakkers, M. Wimmer, and L. P. Kouwenhoven, *Realization of a minimal Kitaev chain in coupled quantum dots*, Nature (London) **614**, 445 (2023).

[36] B. Douçot and L. B. Ioffe, *Physical implementation of protected qubits*, Rep. Prog. Phys. **75**, 072001 (2012).

[37] P. Brooks, A. Kitaev, and J. Preskill, *Protected gates for superconducting qubits*, Phys. Rev. A **87**, 052306 (2013).

[38] T. W. Larsen, M. E. Gershenson, L. Casparis, A. Kringhøj, N. J. Pearson, R. P. G. McNeil, F. Kuemmeth, P. Krogstrup, K. D. Petersson, and C. M. Marcus, *Parity-protected superconductor-semiconductor qubit*, Phys. Rev. Lett. **125**, 056801 (2020).

[39] A. Gyenis, P. S. Mundada, A. Di Paolo, T. M. Hazard, X. You, D. I. Schuster, J. Koch, A. Blais, and A. A. Houck, *Experimental realization of a protected superconducting circuit derived from the* 0-π *qubit*, PRX Quantum **2**, 010339 (2021).

[40] A. H. Pfeffer, J. E. Duvauchelle, H. Courtois, R. Mélin, D. Feinberg, and F. Lefloch, *Subgap Structure in the conductance of a three-terminal Josephson junction*, Phys. Rev. B **90**, 075401 (2014).

[41] Y. Cohen, Y. Ronen, J.-H. Kang, M. Heiblum, D. Feinberg, R. Mélin, and H. Shtrikman, *Nonlocal supercurrent of quartets in a three-terminal Josephson junction*, Proc. Natl. Acad. Sci. U.S.A. **115**, 6991 (2018).

[42] A. W. Draelos, M.-T. Wei, A. Seredinski, H. Li, Y. Mehta, K. Watanabe, T. Taniguchi, I. V. Borzenets, F. Amet, and G. Finkelstein, *Supercurrent flow in multiterminal graphene Josephson junctions*, Nano Lett. **19**, 1039 (2019).

[43] G. V. Graziano, J. S. Lee, M. Pendharkar, C. J. Palmstrøm, and V. S. Pribiag, *Transport studies in a gate-tunable three-terminal Josephson junction*, Phys. Rev. B **101**, 054510 (2020).

[44] N. Pankratova, H. Lee, R. Kuzmin, K. Wickramasinghe, W. Mayer, J. Yuan, M. G. Vavilov, J. Shabani, and V. E. Manucharyan, *Multiterminal Josephson effect*, Phys. Rev. X **10**, 031051 (2020).

[45] E. G. Arnault, T. F. Q. Larson, A. Seredinski, L. Zhao, S. Idris, A. McConnell, K. Watanabe, T. Taniguchi, I. Borzenets, F. Amet, and G. Finkelstein, *Multiterminal inverse ac Josephson effect*, Nano Lett. **21**, 9668 (2021).

[46] K.-F. Huang, Y. Ronen, R. Mélin, D. Feinberg, K. Watanabe, T. Taniguchi, and P. Kim, *Evidence for* 4*e charge of Cooper quartets in a biased multi-terminal graphene-based Josephson junction*, Nat. Commun. **13**, 3032 (2022).

[47] E. G. Arnault, S. Idris, A. McConnell, L. Zhao, T. F. Larson, K. Watanabe, T. Taniguchi, G. Finkelstein, and F. Amet, *Dynamical stabilization of multiplet supercurrents in multi-terminal Josephson junctions*, Nano Lett. **22**, 7073 (2022).

[48] G. V. Graziano, M. Gupta, M. Pendharkar, J. T. Dong, C. P. Dempsey, C. Palmstrøm, and V. S. Pribiag, *Selective control of conductance modes in multi-terminal Josephson junctions*, Nat. Commun. **13**, 5933 (2022).

[49] J. Kölzer, A. R. Jalil, D. Rosenbach, L. Arndt, G. Mussler, P. Schüffelgen, D. Grützmacher, H. Lüth, and T. Schäpers, *Supercurrent in* Bi_4Te_3 *topological material-based three-terminal junctions*, Nanomater. Nanotechnol. **13**, 293 (2023).

[50] F. Zhang, A. S. Rashid, M. T. Ahari, W. Zhang, K. M. Ananthanarayanan, R. Xiao, G. J. de Coster, M. J. Gilbert, N. Samarth, and M. Kayyalha, *Andreev processes in mesoscopic multiterminal graphene Josephson junctions*, Phys. Rev. B **107**, L140503 (2023).

[51] J. Chiles, E. G. Arnault, C.-C. Chen, T. F. Q. Larson, L. Zhao, K. Watanabe, T. Taniguchi, F. Amet, and G. Finkelstein, *Nonreciprocal supercurrents in a field-free graphene Josephson triode*, Nano Lett. **23**, 5257 (2023).

[52] M. Gupta, G. V. Graziano, M. Pendharkar, J. T. Dong, C. P. Dempsey, C. Palmstrøm, and V. S. Pribiag, *Gate-tunable superconducting diode effect in a three-terminal Josephson device*, Nat. Commun. **14**, 3078 (2023).

[53] M. Coraiola, D. Z. Haxell, D. Sabonis, H. Weisbrich, A. E. Svetogorov, M. Hinderling, S. C. ten Kate, E. Cheah, F. Krizek, R. Schott, W. Wegscheider, J. C. Cuevas, W. Belzig, and F. Nichele, *Phase-engineering the Andreev band structure of a three-terminal Josephson junction*, Nat. Commun. **14**, 6784 (2023).

[54] T. Yokoyama and Y. V. Nazarov, *Singularities in the Andreev Spectrum of a Multiterminal Josephson Junction*, Phys. Rev. B **92**, 155437 (2015).
[55] R.-P. Riwar, M. Houzet, J. S. Meyer, and Y. V. Nazarov, *Multi-terminal Josephson junctions as topological matter*, Nat. Commun. **7**, 11167 (2016).
[56] H.-Y. Xie, M. G. Vavilov, and A. Levchenko, *Topological Andreev bands in three-terminal Josephson junctions*, Phys. Rev. B **96**, 161406(R) (2017).
[57] J.-D. Pillet, V. Benzoni, J. Griesmar, J.-L. Smirr, and Ç. O. Girit, *Nonlocal Josephson effect in Andreev molecules*, Nano Lett. **19**, 7138 (2019).
[58] V. Kornich, H. S. Barakov, and Y. V. Nazarov, *Fine energy splitting of overlapping Andreev bound states in multiterminal superconducting nanostructures*, Phys. Rev. Res. **1**, 033004 (2019).
[59] S. Matsuo, J. S. Lee, C.-Y. Chang, Y. Sato, K. Ueda, C. J. Palmstrøm, and S. Tarucha, *Observation of nonlocal Josephson effect on double* InAs *Nanowires*, Commun. Phys. **5**, 221 (2022).
[60] S. Matsuo, T. Imoto, T. Yokoyama, Y. Sato, T. Lindemann, S. Gronin, G. C. Gardner, S. Nakosai, Y. Tanaka, M. J. Manfra, and S. Tarucha, *Phase-dependent Andreev molecules and superconducting gap closing in coherently-coupled Josephson junctions*, Nat. Commun. **14**, 8271 (2023).
[61] D. Z. Haxell, M. Coraiola, M. Hinderling, S. C. ten Kate, D. Sabonis, A. E. Svetogorov, W. Belzig, E. Cheah, F. Krizek, R. Schott, W. Wegscheider, and F. Nichele, *Demonstration of the nonlocal Josephson effect in Andreev molecules*, Nano Lett. **23**, 7532 (2023).
[62] S. Matsuo, T. Imoto, T. Yokoyama, Y. Sato, T. Lindemann, S. Gronin, G. C. Gardner, M. J. Manfra, and S. Tarucha, *Phase engineering of anomalous Josephson effect derived from Andreev molecules*, Sci. Adv. **9**, eadj369 (2023).
[63] C. W. J. Beenakker, *Universal limit of critical-current fluctuations in mesoscopic Josephson junctions*, Phys. Rev. Lett. **67**, 3836 (1991).
[64] E. Cheah, D. Z. Haxell, R. Schott, P. Zeng, E. Paysen, S. C. ten Kate, M. Coraiola, M. Landstetter, A. B. Zadeh, A. Trampert, M. Sousa, H. Riel, F. Nichele, W. Wegscheider, and F. Krizek, *Control over epitaxy and the role of the* InAs/Al *interface in hybrid two-dimensional electron gas systems*, Phys. Rev. Mater. **7**, 073403 (2023).
[65] F. Fan, Y. Chen, D. Pan, J. Zhao, and H. Q. Xu, *Measurements of spin–orbit interaction in epitaxially grown* InAs *nanosheets*, Appl. Phys. Lett. **117**, 132101 (2020).
[66] See Supplemental Material at http://link.aps.org/supplemental/10.1103/PhysRevX.14.031024 for details on materials and methods and additional supporting data (Figs. S1–S15).
[67] H. J. Suominen, M. Kjaergaard, A. R. Hamilton, J. Shabani, C. J. Palmstrøm, C. M. Marcus, and F. Nichele, *Zero-energy modes from coalescing Andreev states in a two-dimensional semiconductor-superconductor hybrid platform*, Phys. Rev. Lett. **119**, 176805 (2017).
[68] R. C. Dynes, V. Narayanamurti, and J. P. Garno, *Direct measurement of quasiparticle-lifetime broadening in a strong-coupled superconductor*, Phys. Rev. Lett. **41**, 1509 (1978).
[69] T. Ihn, *Semiconductor nanostructures: Quantum states and electronic transport*, 2nd ed. (Oxford University Press, New York, 2010).
[70] T. Yokoyama, M. Eto, and Y. V. Nazarov, *Anomalous Josephson effect induced by spin-orbit interaction and Zeeman effect in semiconductor nanowires*, Phys. Rev. B **89**, 195407 (2014).
[71] M. Kjaergaard, F. Nichele, H. J. Suominen, M. P. Nowak, M. Wimmer, A. R. Akhmerov, J. A. Folk, K. Flensberg, J. Shabani, C. J. Palmstrøm, and C. M. Marcus, *Quantized conductance doubling and hard gap in a two-dimensional semiconductor–superconductor heterostructure*, Nat. Commun. **7**, 12841 (2016).
[72] A. Fornieri, A. M. Whiticar, F. Setiawan, E. Portolés, A. C. C. Drachmann, A. Keselman, S. Gronin, C. Thomas, T. Wang, R. Kallaher, G. C. Gardner, E. Berg, M. J. Manfra, A. Stern, C. M. Marcus, and F. Nichele, *Evidence of topological superconductivity in planar Josephson junctions*, Nature (London) **569**, 89 (2019).
[73] M. Coraiola, D. Z. Haxell, D. Sabonis, M. Hinderling, S. C. ten Kate, E. Cheah, F. Krizek, R. Schott, W. Wegscheider, and F. Nichele, *Spin-degeneracy breaking and parity transitions in three-terminal Josephson junctions (v1)*, Zenodo, (2024), 10.5281/zenodo.12752167.